

Glycerol Electrooxidation

Enhancing C—C Bond Cleavage of Glycerol Electrooxidation Through Spin-Selective Electron Donation in Pd–PdS₂–Co_x Heterostructural Nanosheets

Pei Liu⁺, Hao Ma⁺, Yuchen Qin,^{*} Junjun Li, Fengwang Li, Jinyu Ye, Qiudi Guo, Ning Su, Chao Gao, Lixia Xie, Xia Sheng, Shiju Zhao, Guangce Jiang, Yunlai Ren, Yuanmiao Sun,^{*} and Zhicheng Zhang^{*}

Abstract: As a 4d transition metal, the spin state of Pd is extremely difficult to directly regulate for the optimized *d* orbital states owing to the strong spin-orbit coupling effect and further extended *d* orbital. Herein, we devise a “spin-selective electron donation” strategy to tune specific *d* orbital electrons of Pd inspired by the Dewar–Chatt–Duncanson model theory. Co–S–Pd bridges with different spin-states of Co^{III} have been constructed in a series of Pd–PdS₂–Co_x HNSs with tunable Co content. Experiments and theoretical calculations indicate that low-spin Co^{III} (*t*_{2g}⁶*e*_g⁰) with fully occupied *t*_{2g} orbitals and empty *d*_{z² orbitals can accurately alter the *d*_{z² electron of Pd by σ -donation via the Co–S–Pd bridge. In contrast, the unfilled *d*_{xy} orbital of high-spin Co^{III} (*t*_{2g}⁵*e*_g¹) is essential for controlling the *d*_{xy} electron of Pd via π -donation. Benefiting from *d*_{z² state optimization by σ -donation, Pd–PdS₂–Co_{4.0} delivers superior performance toward various bioalcohols (ethanol, ethylene glycol, and glycerol) with enhanced C—C bond cleavage. Furthermore, coupling the glycerol oxidation reaction with the CO₂ reduction reaction (GOR||CO₂RR), the electricity consumption of GOR||CO₂RR drops 46.4% compared to the state-of-art system (OER||CO₂RR). Moreover, anodic Faraday efficiency (FE) of formic acid can be attainable at more than 90% at low voltage regions.}}}

Introduction

Modern molecular orbital bonding theory indicates the *d*_{z² orbital of transition metals generally has robust σ -type}

interaction with intermediates owing to the favorable vertical orientation toward surface-bound intermediates.^[1–3] Thus, the filling of *d*_{z² orbital states effectively governs the strength of surface-adsorbate bonding, resulting in the high impact on catalytic performance.^[4] Previous reports have demonstrated that the filling of *d*_{z² orbital states strongly depends on the spin state of transition metal ions,^[5] and employing the spin-regulation strategy for 3d transition metals (Co, Ni, Fe, etc.) could offer an effective approach to modulate the *e*_g orbitals (*d*_{z² and *d*_{x²–y²) occupancy, improving the electrocatalytic performance toward various reactions such as CO₂ reduction, water splitting, and N₂ fixation.^[6–12]}}}}

Glycerol, a non-valued byproduct of industrial biodiesel, has been regarded as one of the top 12 platform molecules for conversion into high-value chemicals by the U.S. Department of Energy (DOE). In addition to the diversity of value-added products, a significant amount of energy can also be released to feed cell devices with the C—C bond cleavage during the glycerol oxidation reaction (GOR) process, especially when C₁ product such as formic acid (HCOOH) is dominant.^[13–15] Palladium (Pd) based electrocatalysts have shown impressive GOR performance in alkaline media.^[16,17] Unfortunately, the weak capability of Pd to cleave C—C bonds necessitates high working potential and temperature, which in turn impedes the energy output and reduces the formic acid yield.^[18,19] The intrinsic reason lies in the full occupancy of *d*_{z² orbitals at metallic Pd sites, resulting in the weak interaction with pivotal adsorbates for C—C bond cleavage.^[20] Therefore, the development of efficient strategies to precisely tailor *d*_{z²}}

[*] P. Liu⁺, Prof. Y. Qin, Q. Guo, N. Su, C. Gao, Prof. L. Xie, Prof. X. Sheng, S. Zhao, G. Jiang, Prof. Y. Ren
 College of sciences, Henan Agricultural University, Zhengzhou 450000, P.R. China
 E-mail: qinyuchen@henau.edu.cn

J. Li, Prof. Z. Zhang
 Department of Chemistry, School of Science, Tianjin University, Tianjin 300072, P.R. China
 E-mail: zczhang19@tju.edu.cn

H. Ma⁺, Prof. Y. Sun
 Institute of Technology for Carbon Neutrality, Shenzhen Institute of Advanced Technology, Chinese Academy of Sciences, Shenzhen 518055, P.R. China
 E-mail: sunym@siat.ac.cn

J. Ye
 Key Laboratory of Physical Chemistry of Solid Surfaces, college of Chemistry and Chemical Engineering, Xiamen University, Xiamen, Fujian 361005, P.R. China

Prof. F. Li
 School of Chemical and Biomolecular Engineering and ARC Centre of Excellence for Green Electrochemical Transformation of Carbon Dioxide, The University of Sydney, Sydney, NSW 2006, Australia

[†] Both authors contributed equally to this work.

Additional supporting information can be found online in the Supporting Information section

orbital occupancy of Pd sites is the key to enhancing the C–C bond cleavage and facilitating superior reaction kinetics.

However, as a 4d transition metal, Pd exhibits a stronger spin-orbit coupling effect and further extended *d* orbitals when compared to 3d transition metals.^[21–23] These characteristics make it extremely challenging to modulate the spin state of Pd, thereby making it impossible to directly change the d_{z^2} occupation. On the other hand, a stronger spin-orbit coupling effect and extended *d* orbitals simultaneously endow Pd compounds with abundant quantum phases and topological states, making the electronic structure of Pd sites more sensitive to intrinsic physics and external fields.^[24] Thus, tuning the lattice structure of Pd sites and creating effective electron transport pathways could exhibit great potential to tailor the d_{z^2} orbital occupancy of Pd sites.

Complexes with dative bonds are susceptible to charge-transfer frustration due to the mixing of ionic and covalent potential energy surfaces. The Dewar–Chatt–Duncanson model describes metal-ligand interactions leading to the forward donation from the ligand to the metal, where the *d* orbital states of the metal play a significant role in determining the donation type.^[25] Unfilled t_{2g} orbitals and ligands' p orbitals tend to form π -donation. Conversely, the formation of σ -donation occurs when the empty d_{z^2} orbital interacts with the p orbital of ligands.^[26] Enlightened by this theoretical framework, we try to capitalize on the malleability of spin states in cobalt (Co) and the responsiveness of Pd complexes (PdS_2) to propose the concept and strategy of “spin-selective electron donation.” By regulating the spin state of Co, various types of donations are induced in Co–S–Pd bond, resulting in precise modulation of the d_{z^2} orbital state of Pd sites.

Herein, we fabricated Pd–PdS₂–Co_x heterostructural nanosheets (HNSs) with three different contents of single atomic Co (Pd–PdS₂–Co_{2.8}, Pd–PdS₂–Co_{4.0}, and Pd–PdS₂–Co_{5.2}). Theoretical calculations with crystal field theory (CFT) demonstrate that the single atomic Co decoration causes the lattice distortion, leading to the modulation of the d_{z^2} orbital state of Pd sites. However, Pd–PdS₂–Co_{2.8}, Pd–PdS₂–Co_{4.0}, and Pd–PdS₂–Co_{5.2} exhibit significantly different performances toward the bio-alcohols (ethanol, ethylene glycol, and glycerol) electrooxidation, indicating that the lattice distortion is not the dominant reason in orbital state modification. Temperature-dependent magnetization measurements reveal that Co^{III} in Pd–PdS₂–Co_x HNSs possesses different spin states, i.e., high spin (HS, $t_{2g}^5e_g^1$) state and low spin (LS, $t_{2g}^6e_g^0$) state. Based on theoretical calculations and CFT, “spin-selective electron donation” concept is proposed in our work. Specifically, Co–LS with fully occupied t_{2g} orbitals and empty e_g orbitals can precisely alter the d_{z^2} state of Pd by σ -donation in the Co–S–Pd bridge, while unfilled d_{xy} orbitals of Co–HS are essential for controlling the d_{xy} state of Pd via π -donation. Density functional theory (DFT) calculations and in situ Fourier transform infrared spectroscopy (FTIR) confirm that the modulated d_{z^2} state of Pd–PdS₂–Co_{4.0} by Co–LS is beneficial for GOR to HCOOH. As a proof-of-concept application, Pd–PdS₂–Co_{4.0} (anodic catalysts) delivers the lowest energy consumption and superior HCOOH production in coupling GOR with the electrochemical carbon dioxide reduction reaction (GOR||CO₂RR) system. Compared to

the conventional CO₂RR system (OER||CO₂RR), the cell voltage of GOR||CO₂RR on Pd–PdS₂–Co_{4.0} drops by 1.09 V at the current density of 5 mA cm^{−2}, leading to a drastic reduction in the electricity consumption by approximately 46.4%. Meanwhile, the high Faraday efficiency (FE) of HCOOH can be achieved at anode about 90% at the low cell potential region.

Results and Discussion

Considering the e_g states of Pd are sensitive to perturbations in crystal structures,^[2] the single atomic Co atoms are decorated to construct the local lattice distortion in PdS₂. Theoretical calculations were employed to investigate the e_g states change of Pd sites after the incorporation of single atomic Co. As expected, the Co-decorated PdS₂ model (PdS–Co, atomic ratio of Pd:S:Co = 23:48:1) displays an obvious lattice distortion after geometry optimization (Figure S1). The projected density of states (PDOS) was patterned to illustrate the *d*-orbital states of Pd in PdS₂ and PdS–Co (Figure S2), in which an evident difference can be identified. As depicted, in PdS₂–Co, the d_{z^2} orbital is sharp and lies below the Fermi level, while $d_{x^2-y^2}$ orbital is wide and crosses the Fermi level. The situation in PdS₂ is, however, totally different, in which the d_{z^2} orbital is wide and crosses the Fermi level while the $d_{x^2-y^2}$ orbital is sharp and lies below the Fermi level. These results indicate that e_g orbital states of Pd alter dramatically between PdS₂ and PdS₂–Co. Moreover, the electron configurations of Pd *d*-orbital were further investigated via combining PDOS and CFT analysis. As shown in Figure 1, in PdS₂, the d_{z^2} orbital is empty ($d_{z^2}^0$) and its energy state is higher than the fully occupied $d_{x^2-y^2}$ orbital ($d_{x^2-y^2}^2$). As a comparison, the incorporation of single atomic Co induces lattice distortion in PdS₂–Co. As a result, the energy state of d_{z^2} orbital drops below that of the $d_{x^2-y^2}$ orbital and the two electrons on e_g orbitals are equally divided to separately occupy the d_{z^2} and $d_{x^2-y^2}$ orbitals ($d_{z^2}^1, d_{x^2-y^2}^1$) in PdS₂–Co. These theoretical insights demonstrate that it is feasible to tailor the e_g orbital states of Pd sites by introducing single atom Co.

Based on the above-mentioned theoretical calculation results, we synthesized Pd–PdS₂ and Pd–PdS₂–Co_x (*x* is the Co mass fraction) with different Co amounts, referring to our previous method for preparing Pd–PdSe HNSs.^[19] According to the results of X-ray Fluorescence (XRF), the as-prepared Pd–PdS₂–Co_x with Co mass fractions of 2.8%, 4.0%, and 5.2% were named Pd–PdS₂–Co_{2.8}, Pd–PdS₂–Co_{4.0}, and Pd–PdS₂–Co_{5.2}, respectively. The representative transmission electron microscopy (TEM) images display that both Pd–PdS₂ and Pd–PdS₂–Co_x are typical two-dimensional (2D) nanosheets with an average lateral size of around 100 nm (Figure S3). The powder X-ray diffraction (XRD) patterns of as-prepared Pd–PdS₂ and Pd–PdS₂–Co_x both show the characteristic diffraction signals of PdS₂ and Pd phases, demonstrating the possible heterostructure of Pd–PdS₂ and Pd–PdS₂–Co_x (Figure S4). In addition, X-ray photoelectron spectroscopy (XPS) demonstrates that the ratio of oxidized state (Pd²⁺) is around 45% for both Pd–PdS₂ and Pd–PdS₂–Co_x, indicating

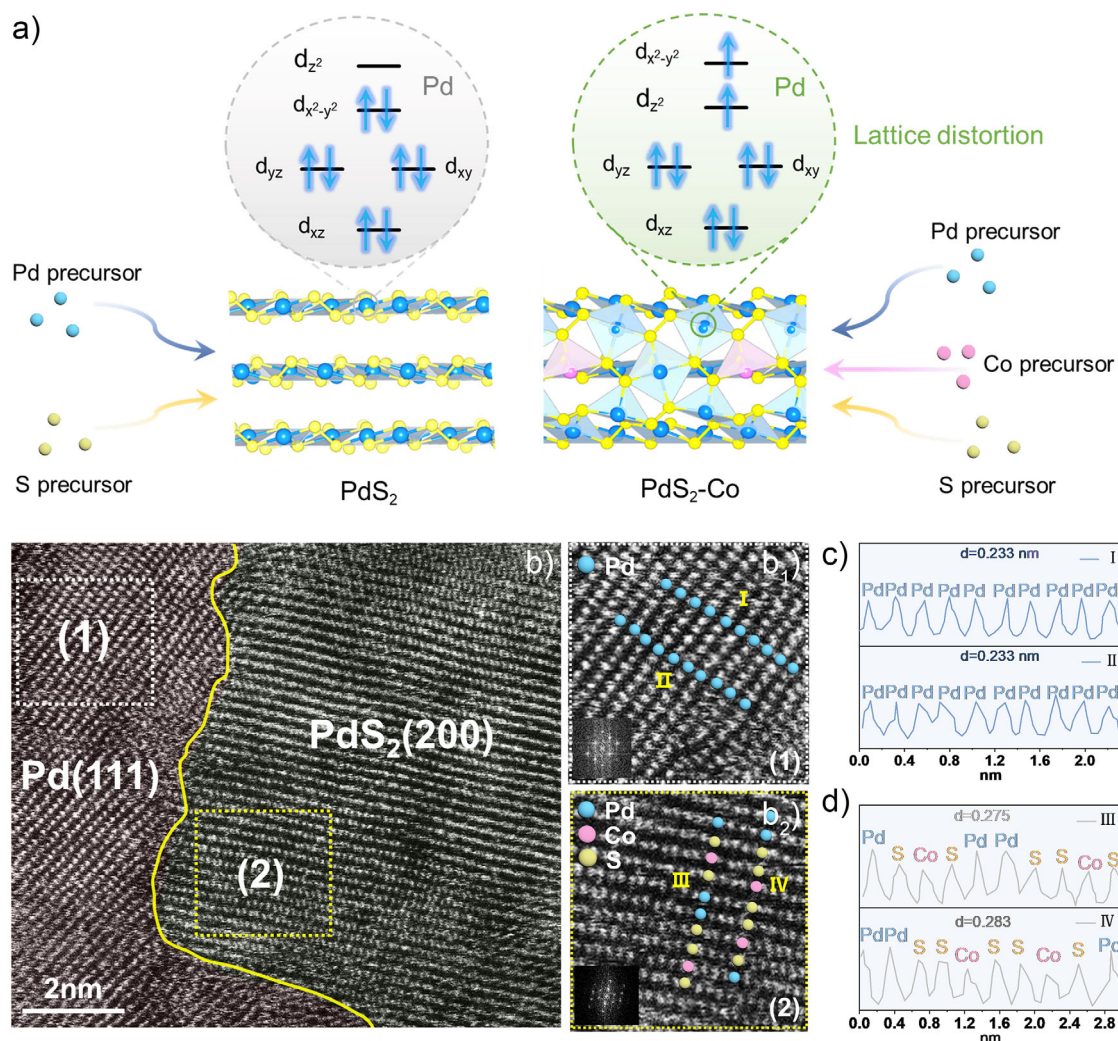


Figure 1. a) Lattice distortion can induce different Pd *d*-orbital states of PdS₂ and PdS₂-Co models. b) Aberration-corrected STEM image of Pd-PdS₂-Co_{4.0}. c) and d) The intensity profile and calculated average *d*-spacing of (111) and (200) planes from Pd (111) and PdS₂ (200) in (b₁) and (b₂), respectively.

the similar component of PdS₂ and Pd phases (Figure S5). Additionally, Pd *K*-edge X-ray absorption near edge structure (XANES) measurements were performed for both Pd-PdS₂ and Pd-PdS₂-Co_x (Figure S6). The Pd *K*-edge XANES spectra reveal that the valence state of Pd in both Pd-PdS₂ and Pd-PdS₂-Co_x lies between 0 and +2, confirming the coexistence of metallic and oxidized states.

To further analyze the lattice structure and heterostructure of Pd-PdS₂-Co_x at the atomic level, Pd-PdS₂-Co_{4.0} has been chosen as a reference material. High-angle annular dark-field scanning transmission electron microscopy (HAADF-STEM) and atomic force microscopy (AFM) images reveal an average thickness of approximately 3 nm for Pd-PdS₂-Co_{4.0} nanosheets (Figure S7a,b). STEM elemental mapping confirms the uniform distribution of Pd, Co, and S elements throughout the nanosheet (Figure S7c). Aberration-corrected STEM has been utilized to provide a more detailed insight into the lattice structure. In Figure S8, it is evident that different lattice spacings (*dm*) are present in various regions

of the Pd-PdS₂-Co_{4.0}. The *dm* in the left region is measured to be approximately 0.232 ± 0.002 nm with a minimal fluctuation range, indicating the presence of the Pd (111) facet with a face-centered cubic (*fcc*) phase. Conversely, the average *dm* in the right region is around 0.276 ± 0.008 nm, suggesting the dominance of the PdS₂ (200) phase. These results demonstrate that Pd-PdS₂-Co_{4.0} possesses the heterostructure of metallic Pd and PdS₂ phases (Figure 1b), which is in close agreement with the results of XRD. It is worth noting that the *dm* of the PdS₂ region displays a high fluctuation from 0.268 to 0.284 nm, suggesting the lattice distortions in the PdS₂ (200) phase. Moreover, the integrated pixel intensities for heterostructure lattices from different selected areas (Figure 1b₁,b₂) in Pd-PdS₂-Co_{4.0} are shown in Figure 1c,d. The assignment of Pd, Co, and S atoms in Figure 1d is a speculation based on the Fourier transformed extended X-ray absorption fine structure (FT-EXAFS) results (see more details in Figure S9). The integrated pixel intensities of metallic Pd (111) show a negligible fluctuation, revealing that Pd atoms dominate

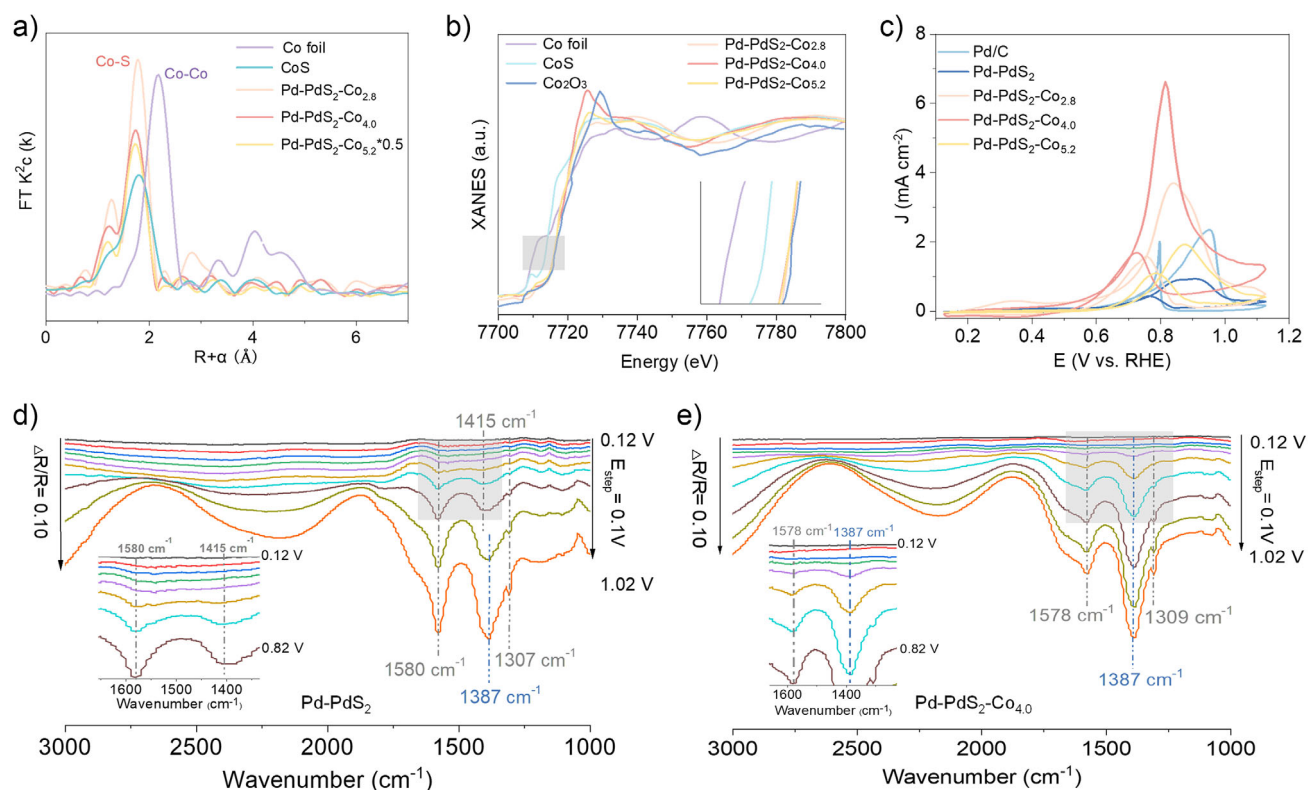


Figure 2. a) Fourier-transformed Co *K*-edge EXAFS spectra, b) Co *K*-edge XANES spectra. c) Cyclic voltammogram curves of various catalysts in 1 M KOH+0.1 M glycerol. In situ FTIR spectra of GOR on d) Pd-PdS₂ and e) Pd-PdS₂-Co_{4.0}.

in this region. In contrast, PdS₂ phase displays a drastic fluctuation of integrated pixel intensity, suggesting that Co atoms are mainly doped in this phase. Combining it with the high fluctuation range of Δm in the PdS₂ phase, it is reasonable to conclude that Co decorated in the PdS₂ phase successfully induces the lattice distortions.

The local atomic and electronic structure of Pd-PdS₂-Co_x HNSs has been further revealed by X-ray absorption fine-structure spectroscopy (XAFS). The FT-EXAFS spectra of Pd-PdS₂-Co_{2.8}, Pd-PdS₂-Co_{4.0} and Pd-PdS₂-Co_{5.2} possess peaks at ~ 1.7 Å, which could be assigned to the Co-S bond (Figure 2a). Note that, no Co-Co peak was observed for Pd-PdS₂-Co_{2.8}, Pd-PdS₂-Co_{4.0} and Pd-PdS₂-Co_{5.2}, confirming the successful synthesis of atomically dispersed Co in Pd-PdS₂-Co_x HNSs, which is consistent with the results of aberration-corrected STEM. Figure S10 presents the fitting results, while the corresponding structural parameters, including bond lengths and coordination numbers (CNs) are summarized in Table S1. The CN of Co-S in all three Pd-PdS₂-Co_x HNSs samples is approximately 4.0, suggesting that single-atom Co substitutes for Pd within the PdS₂ lattice. Moreover, the Co *K*-edge XANES of Pd-PdS₂-Co_{4.0} and Pd-PdS₂-Co_{2.8} both display rising edge energy similar to that of standard Co₂O₃, demonstrating the oxidation state of Co species is approximately +3. Pd-PdS₂-Co_{5.2} exhibit a slight negative shift in comparison with Co₂O₃, illustrating the lower oxidation state of Co (Figure 2b). Combining the XAFS with TEM results, we may conclude that single atomic Co has been

successfully introduced in the PdS₂ phase of Pd-PdS₂-Co_x HNSs, leading to the lattice distortions.

As a proof-of-concept application, the electrocatalytic performances of Pd-PdS₂-Co_x HNSs toward bio-alcohols (ethanol, ethylene glycol, and glycerol) oxidation was measured in alkaline media by a three-electrode system. Moreover, Pd-PdS₂ and commercial Pd/C were chosen as the reference catalysts. The electrochemical surface areas (ECSAs) were determined by integrating the columbic charge of PdO reduction at ~ 0.7 V (RHE) in cyclic voltammetry (CV) curves measured in 1 M KOH (Figure S11). Herein, Pd-PdS₂-Co_{4.0} (52.7 m² g⁻¹) exhibits a similar ECSA to Pd-PdS₂-Co_{2.8} (51.8 m² g⁻¹), both of which are higher than that of commercial Pd/C (43.6 m² g⁻¹), Pd-PdS₂-Co_{5.2} (33.9 m² g⁻¹), and Pd-PdS₂ (27.4 m² g⁻¹). The specific activities of ethanol oxidation reaction (EOR), ethylene glycol oxidation reaction (EGOR) and GOR on various catalysts were measured. Figures 2c and S12-S14 show the specific activities of GOR, EOR, and EGOR. Among these catalysts, Pd-PdS₂-Co_{4.0} delivered the highest catalytic activity, and the specific activities of GOR (EOR and EGOR) are about 2.85 (5.74 and 5.30) and 7.20 (5.78 and 2.67) times those of commercial Pd/C and Pd-PdS₂, respectively. However, the catalytic activities of Pd-PdS₂-Co_{2.8} and Pd-PdS₂-Co_{5.2} are unsatisfactory in comparison with Pd-PdS₂-Co_{4.0}. Additionally, the ratios of the forward current (*I*_f) to the reverse current (*I*_b) of Pd-PdS₂ and Pd-PdS₂-Co_x HNSs are significantly higher than those of commercial Pd/C (Figure S15),

suggesting the excellent oxidation removal ability of CO intermediates.^[27]

Besides the catalytic activity, the C–C bond breaking ability of electrocatalysts is another crucial factor for carbon atom utilization and energy conversion efficiency during bio-alcohol electrooxidation. To obtain the information of C–C bond cleavage in the surface micro-environment on Pd–PdS₂–Co_x HNSs, electrochemical in situ FTIR measurement was carried out. Figures S16 and S17 show the complete FTIR spectra of EOR from 0.12 to 1.32 V (vs. RHE) at an interval of 0.1 V. All electrocatalysts display two strong downward characteristic bands at 1550 and 1414 cm^{−1}, corresponding to the asymmetric and symmetric stretching vibrational modes of O–C–O in CH₃COO[−] ions, demonstrating the presence of C₂ products (CH₃COO[−]) without C–C bond cleavage. However, Pd–PdS₂–Co_x HNSs show distinct differences with Pd–PdS₂ and standard IR characteristic peaks of CH₃COO[−] (Figure S18). The enhanced intensity of 1414 cm^{−1} band suggests that numerous CO₃^{2−} ions are produced on Pd–PdS₂–Co_x HNSs, which causes a band at 1390 cm^{−1} overlapping with that at 1414 cm^{−1}. Especially on Pd–PdS₂–Co_{4.0}, the band intensity of 1414 cm^{−1} is even higher than that of 1550 cm^{−1}, indicating the greater generation of CO₃^{2−} ions caused by the excellent ability of C–C bond cleavage.^[28]

Except for EOR, the in situ FTIR spectra of GOR from 0.12 to 1.22 V (vs. RHE) at an interval of 0.1 V were also conducted (Figures 2d,e, and S19). The upward peak in the region of 1100–1000 cm^{−1} is attributed to the glycerol consumption. The band at ~1308 cm^{−1} is the C–O stretch of the oxalate ion. The characteristic peak at ~1580 cm^{−1} is asymmetric stretch of COO[−]. The broadband at ~1387 cm^{−1} belongs to the symmetric stretching of COO[−] or CO₃^{2−} ions, which presumably overlap with the C–O stretch of formate (~1350 cm^{−1}).^[17,29,30] As shown in Figure 2d, the peaks located at 1415 and 1585 cm^{−1} occur at 0.62 V (vs. RHE), indicating that glycerol molecules are first oxidized to glyceric acid on Pd–PdS₂. Then, the band of 1415 cm^{−1} downshifts to 1387 cm^{−1} as the potential increases, suggesting that the C–C bond starts to break and produce more C₁ products (formate and carbonate). The FTIR results mentioned above suggest that the terminal hydroxyl groups are initially oxidized to form multi-carbon carboxylic acids, such as glycerate, followed by the C–C bond cleavage to generate C₂ products (such as glycolate and oxalate) and C₁ products (formate and carbonate) (Figure S20). However, no negative shift of 1415 to ~1387 cm^{−1} can be observed on Pd–PdS₂–Co_x HNSs, demonstrating the dissociation of C–C bond happens at the beginning of the GOR process. It is worth noting that the band of 1387 cm^{−1} can be detected at 0.42 V (vs. RHE) on Pd–PdS₂–Co_{4.0}, a lower value compared to Pd–PdS₂–Co_{2.8} and Pd–PdS₂–Co_{5.2} at 0.62 V (vs. RHE). This result confirms that Pd–PdS₂–Co_{4.0} has the strongest ability of C–C bond cleavage for GOR, which is in good agreement with the results of FTIR spectra on EOR. The above experimental results reveal an interesting phenomenon that is worth studying. Pd–PdS₂–Co_x HNSs possess similar geometric/lattice structures and compositions but display a wide variety of catalytic activity and C–C bond cleavage ability for EOR and GOR. Thus, we speculate

that there is an uncommon factor affecting the catalytic performance.

Co^{III} has different electron configurations, i.e., t_{2g}⁶e_g⁰ and t_{2g}⁵e_g¹, which are associated with its LS and HS states, respectively.^[31] LS and HS of Co have been demonstrated to cause different local magnetic characteristics around active sites (Pd), potentially modulating the *d*-orbitals states of Pd. To reveal the spin structures of Co^{III} in Pd–PdS₂–Co_x HNSs, temperature-dependent magnetic moments were measured. As shown in Figure 3a, the magnetic behavior supports the paramagnetic feature of these three Pd–PdS₂–Co_x HNSs above 150 K. According to the Curie–Weiss law, the effective magnetic moments (μ_{eff}) could be obtained by fitting the magnetic susceptibilities.^[32] (Figures 3b and S21). Figure 3c shows μ_{eff} of Pd–PdS₂–Co_{2.8}, Pd–PdS₂–Co_{4.0}, and Pd–PdS₂–Co_{5.2} are 2.52, 1.59, and 2.67 μ_{B} , respectively. Based on the relationship between the μ_{eff} and spin states, the spin states of Co^{III} in Pd–PdS₂–Co_{2.8}, Pd–PdS₂–Co_{4.0}, and Pd–PdS₂–Co_{5.2} can be calculated as 20.6% LS + 79.4% HS, 68.4% LS + 31.6% HS and 10.9% LS + 89.1% HS (Figure 3d), respectively. Obviously, Co ions in Pd–PdS₂–Co_{4.0} possess the highest percentage of LS, indicating the lowest e_g electron number and most unoccupied e_g orbitals. Moreover, XANES at Co *L*-edges consistently shows that the oxidation state of Co ions in Pd–PdS₂–Co_x HNSs is +3 (Figure 3e). L3 peak is further carefully deconvoluted into two separate peaks from the t_{2g} and e_g orbitals due to the crystal-field splitting of the neighboring ions.^[33] Moreover, the intensities of these two peaks are direct criteria for the total unoccupied Co 3*d* states.^[34] After integrating the areas of the e_g and t_{2g} peaks, Pd–PdS₂–Co_{4.0} presents the largest area ratio ($A_{\text{eg}}/A_{\text{t2g}}$) of 1.24, which is higher than that of Pd–PdS₂–Co_{2.8} (1.02) and Pd–PdS₂–Co_{5.2} (0.92). This result demonstrates that Co in Pd–PdS₂–Co_{4.0} has a higher density of e_g unoccupied states than others, corresponding to the calculated results of temperature-dependent susceptibility.

DFT calculations were performed to gain insights into the effect of Co^{III} spin states on *d*-orbitals of Pd sites. Based on the results of lattice plane analysis by TEM, single Co atom doped on PdS₂ (200) facet is treated as our research model. Theoretically, the six electrons of the Co^{III} ion can arrange themselves in various occupation configurations among the five *d*-orbitals (*d*_{xy}, *d*_{yz}, *d*_{xz}, *d*_{z²}, and *d*_{x²−y²}), resulting in different electronic spin states. PDOS plots of PdS₂–Co system under HS and LS states of Co^{III} are shown in Figure 4a–d. Based on the CFT analysis, the efficient introduction of Co atoms and the absence of axial ligands (S atoms), the *d*_{x²−y²} orbital state of the Co is higher than the *d*_{z²} orbital, while the energy state of the *d*_{xz} is lower than that of the *d*_{xy} and *d*_{yz}. In the LS state of Co^{III} (Co–LS), the *d*_{xz}, *d*_{xy}, and *d*_{yz} states are fully occupied (Figure 4a). However, the *d*_{x²−y²} states mainly lie above the Fermi level, resulting in an unoccupied configuration of the *d*_{x²−y²} orbitals at the high energy state level. By contrast, in the HS state of Co^{III} (Co–HS), one electron upshifts from *d*_{xy} to *d*_{z²}, resulting in the partial occupancy in both *d*_{xy} and *d*_{z²} orbitals (Figure 4c). Spin density plots in insets (Figure 4a,c) show that Co^{III} in the HS state has a clear spatial distribution of spin electron density compared to the LS state of Co^{III}.

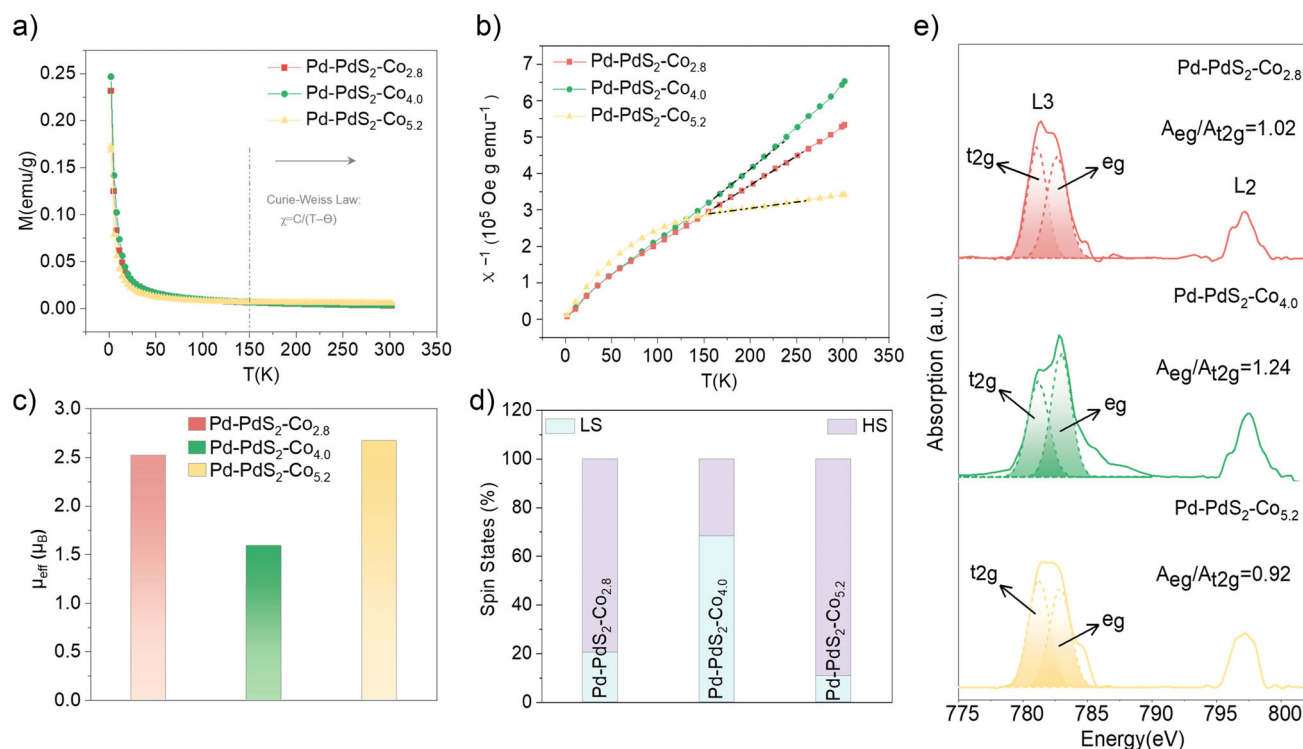


Figure 3. a) Temperature-dependent magnetic moments of Pd–PdS₂–Co_x HNSs under H = 2 kOe. b) Fitted susceptibility vs. temperature based on Curie–Weiss law for Pd–PdS₂–Co_x HNSs. c) The μ_{eff} and d) spin states percentage of Pd–PdS₂–Co_x HNSs. e) Co L-edge XANES spectra of Pd–PdS₂–Co_x HNSs.

The crystal orbital Hamilton population (COHP) analysis confirms that the introduction of Co–LS and Co–HS into PdS₂ both fosters a strong interaction among Co, S, and Pd, forming a Co–S–Pd backbone for electron transfer (Figures S22 and S23). The electronic states of Pd t_{2g} orbitals are primarily distributed below the Fermi level, manifesting the electronic occupation feature (Figure 4b,d). Furthermore, electron contributions across different Pd 4d orbitals with the corresponding electron occupation within Pd 4d orbitals were calculated. As shown in Figure 4e, the d_{z^2} electron percentage of Pd_{Co-LS} (18.2%) reduces significantly compared to Pd_{Co-HS} (20.6%), whereas the electron percentage of d_{xy} (21.8%) in Pd_{Co-LS} is obviously higher than that of Pd_{Co-HS} (19.7%). The above results strongly indicate that different spin states of Co^{III} can modulate various d orbitals occupancy states of Pd via the Co–S–Pd bridge. Integrating the above insights and based on Dewar–Chatt–Duncanson model theory, the mechanism of spin-selective electron donation can be inferred (Figure 4f). π -donation is formed between Co–HS and S owing to the half-filled state of d_{xy} in Co–HS, instigating the d_{xy} electrons transfer from Pd to Co. In contrast, the full occupancy t_{2g} and empty d_{z^2} of Co–LS result in the σ -donation, thereby causing the migration of Pd d_{z^2} electrons via Co–S–Pd bridge. To further visualize the electron transfer mechanism, we calculated the charge density difference for both Co–LS and Co–HS configurations (Figure S24). In the Co–LS system, the results show electron depletion around the Pd d_{z^2} orbital and corresponding accumulation at the Co d_{z^2} site across the S bridge, indicative of σ -donation. Conversely,

the Co–HS system displays electron delocalization between Pd d_{xy} and Co d_{xy} orbitals, supporting a π -donation pathway. These results visually confirm the spin-selective electron donation mechanism at the atomic level.

To shed light on the performance of GOR in relation to the effect of spin-selective electron donation, DFT calculations were conducted on these three typical models including PdS₂ (200), Co–HS/PdS₂ (200) and Co–LS/PdS₂ (200) surfaces. Figure S25 illustrates the electrocatalytic conversion of glycerol to formic acid, which proceeds through a series of key intermediate steps. The process begins with the oxidation of glycerol (C₃H₈O₃) on the electrocatalyst surface, where it is first converted into glyceraldehyde (C₃H₆O₃), accompanied by the transfer of two electrons and two hydroxide ions (OH[−]). Glyceraldehyde then undergoes further oxidation to form glyceric acid (C₃H₆O₄). Finally, glyceric acid is oxidized to formic acid (HCOOH), with the transfer of four electrons and four hydroxide ions (OH[−]). According to the Sabatier principle, achieving an intermediate adsorption strength for catalytic reactions is crucial. Thus, a detailed calculation of the adsorption energies of C₃H₈O₃ and HCOOH was performed. The results in Figure 5a indicate that PdS₂ (200) exhibits the highest adsorption energy for C₃H₈O₃ (−2.94 eV), which can be attributed to the empty Pd d_{z^2} orbital ($d_{z^2}^0$). After introducing one electron into the Pd d_{z^2} orbital ($d_{z^2}^1$) due to the incorporation of Co–HS into the PdS₂ lattice, the adsorption energy of C₃H₈O₃ decreases significantly on Co–HS/PdS₂ (200), with a notably weakened value of −0.50 eV. Different from that of Co–HS, the state of Pd d_{z^2}

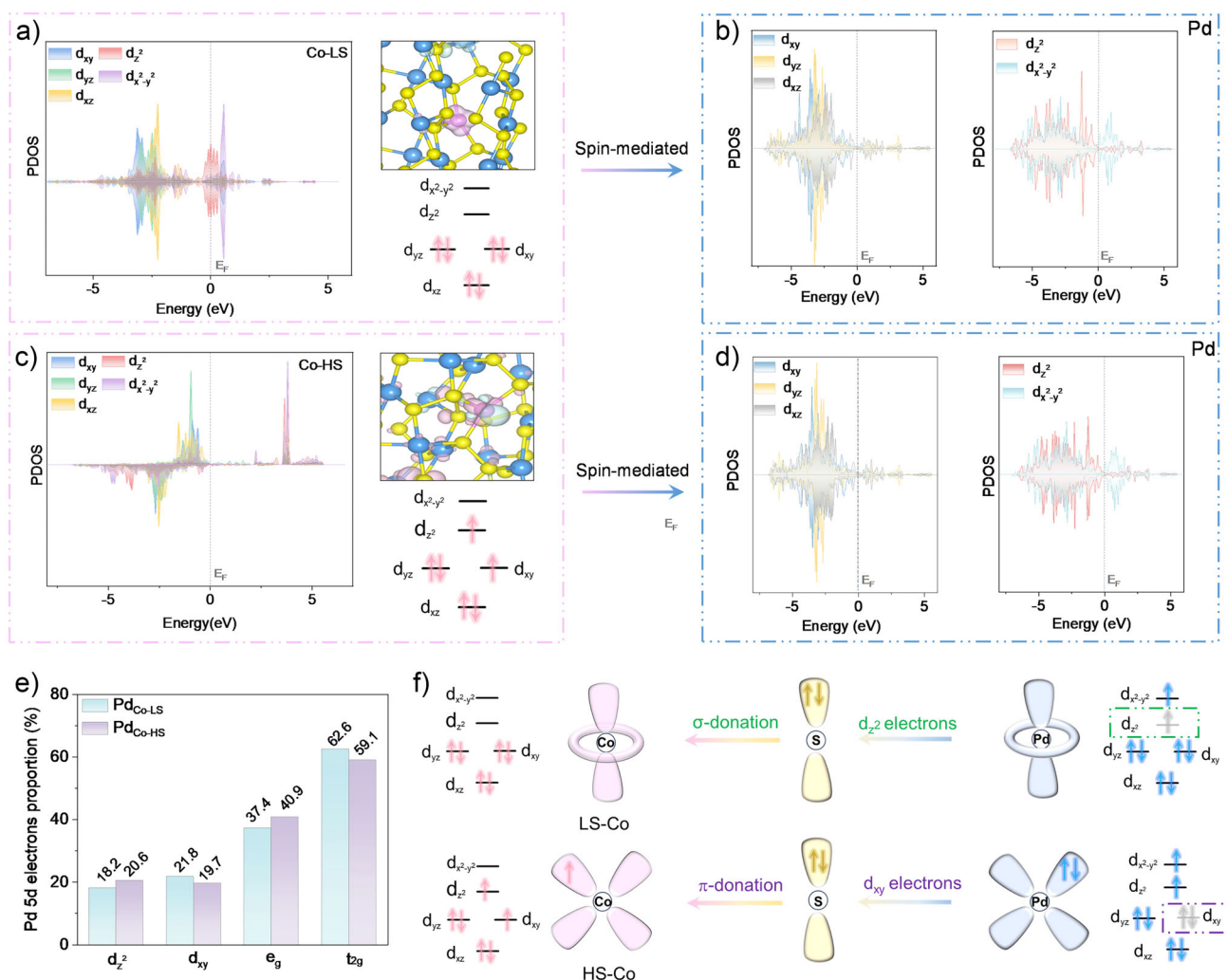


Figure 4. a) Total density of states and PDOS and spin density plots of Co^{III} with low spin state (Co-LS). b) The PDOS of Pd near Co-LS. c) PDOS and spin density plots of Co^{III} with high spin state (Co-HS). d) The PDOS of Pd near Co-HS. e) Calculated Pd 4d PDOS and f) the schematic illustration of the spin-selective electron donation mechanism.

orbital in Co-LS/PdS₂ (200) has been further optimized via σ -donation, resulting in the transfer of d_{z^2} electrons from the Pd actives to Co-LS. This optimization leads to the moderate adsorption strength of C₃H₈O₃ (−1.09 eV) on Co-LS/PdS₂ (200), thereby favoring the GOR process. Meanwhile, the adsorption of HCOOH on Co-LS/PdS₂ (200) significantly decreases in comparison with that on PdS₂ (200), which can promote the rapid desorption of the product. Subsequently, the reaction energy profiles of C₁ pathways toward GOR were also investigated. The implicit solvation correction is taken into consideration in the free energy calculations. As shown in Figure 5b, the rate determining step (RDS) in PdS₂ (200) is HCOOH desorption, which exhibits a large energy barrier of 3.01 eV. This finding indicates that the strong adsorption of HCOOH on the PdS₂ (200) hinders the GOR process. After the introduction of Co into PdS₂, the desorption of HCOOH transitions to an exothermic step, with the RDS being the cleavage of the C–C bond in C₃H₆O₄ to form HCOOH on both Co-LS/PdS₂ and Co-HS/PdS₂. Specifically, on Co-LS/PdS₂ (200), the energy barrier for the RDS is

only 0.65 eV, which is significantly lower than that on Co-HS/PdS₂ (200), indicating a superior ability for C–C bond breaking. These results demonstrate that the optimization of the d_{z^2} state of Pd by Co-LS through σ -donation has significant potential in the conversion of glycerol to formic acid. In addition, ab initio molecular dynamics (AIMD) simulations are further performed at 300 K for 5 ps to evaluate the dynamic stability and potential surface reconstruction of the active site (Figure S26). The results reveal that the overall surface structure remains well preserved throughout the simulation. Notably, the local coordination environments of both Co and Pd centers exhibit no significant distortion.

As indicated by the previous reports,^[13] coupling anodic GOR involved strong C–C bond cleavage with cathodic CO₂RR is an attractive way to significantly reduce the CO₂ electro-reduction cell potential and improve the value-added product (such as HCOOH). To assess the practicality of as-prepared Pd-PdS₂-Co_{4.0} with a strong ability of GOR to HCOOH, we performed an experimental electroanalytical evaluation of GOR||CO₂RR in an H-type cell (Figure 5c).

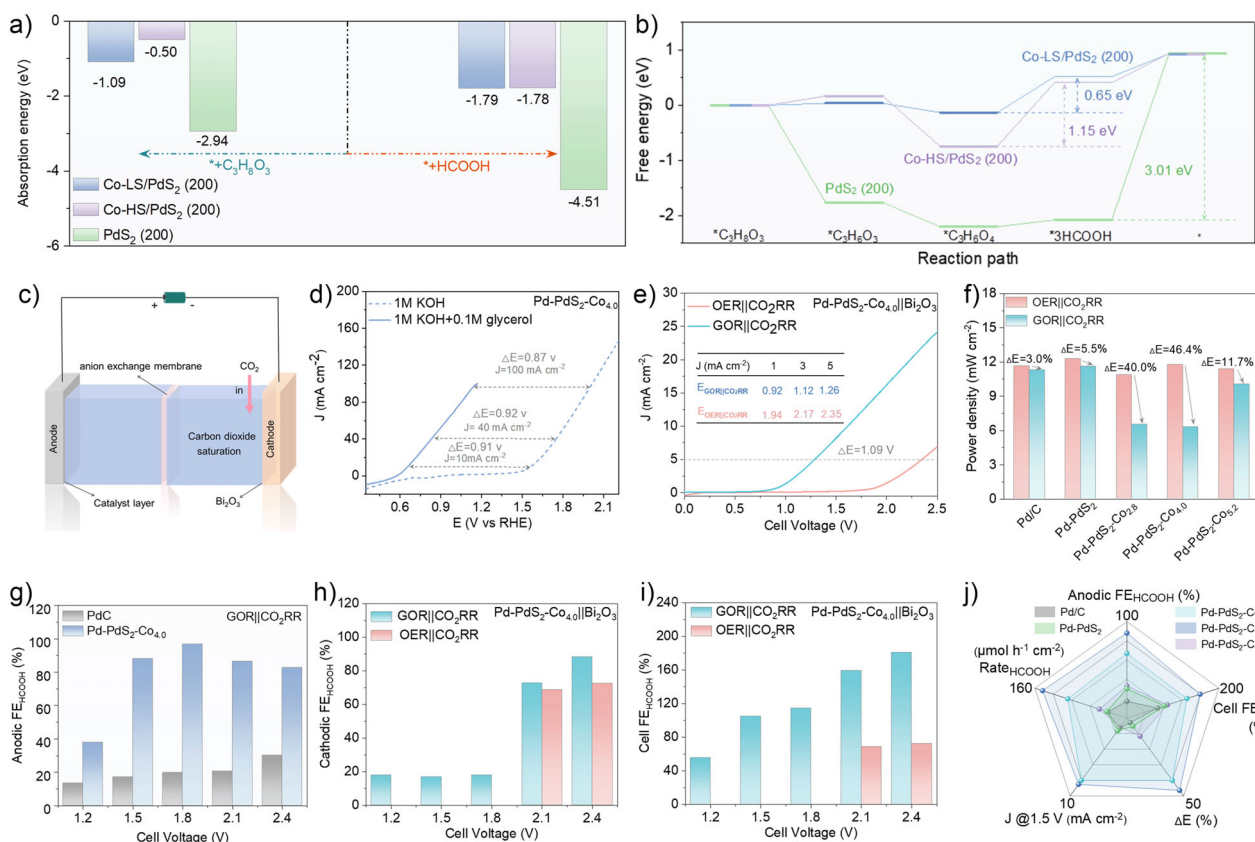


Figure 5. a) The adsorption energy of glycerol and formic acid on three models and b) free energy diagram of glycerol electrooxidation to formic acid pathway on three models. c) Scheme of integrated electrolysis cell. d) The anodic LSV curves of Pd-PdS₂-Co_{4.0}. e) The LSV curves of the integrated cell on Pd-PdS₂-Co_{4.0}. f) The power density of the integrated cell at a current of 5 mA cm⁻². g) The anodic FE of HCOOH in GOR coupling with CO₂RR on Pd-PdS₂-Co_{4.0} and Pd/C. h) The cathodic and i) integrated cell FE of HCOOH on Pd-PdS₂-Co_{4.0}. j) Overall performance comparison among various electrocatalysts.

Pd-PdS₂, Pd-PdS₂-Co_{2.8}, Pd-PdS₂-Co_{5.2}, and commercial Pd/C have been chosen as the reference anodic catalysts, and commercial Bi₂O₃ is employed as the cathodic catalysts. The catalytic performance of GOR were evaluated in a three-electrode H-type electrolytic cell setup. Figures S27 and S28 show the linear sweep voltammetry (LSV) curves measured with or without 0.1 mol glycerol in 1 M KOH solution. Among these catalysts, Pd-PdS₂-Co_{4.0} shows the superior catalytic properties in terms of overpotential and current density. The potential at a current density of 10 mA cm⁻² between GOR and oxygen evolution reaction (OER) exhibits the largest decrease of ~0.91 V. Moreover, the potential drop of GOR has been consistently maintained around 0.9 V at different current densities, indicating that GOR is more favorable than OER on Pd-PdS₂-Co_{4.0}. Meanwhile, Figures S28 and S29 show the cathodic LSV curves of electrochemical CO₂ reduction in 0.5 mol KHCO₃ over Bi₂O₃ with different anodic catalysts. Higher current densities can be observed in a saturated CO₂ atmosphere compared to a N₂ atmosphere in all these cell devices, highlighting the significant CO₂RR performance of Bi₂O₃. Furthermore, the performances for GOR||CO₂RR and traditional OER||CO₂RR on various catalysts were obtained on this H-type Cell device. As shown in Figures 5e and S30, the LSV curves of GOR||CO₂RR validate the advantages of GOR in lowering the cell potential. In

comparison with other catalysts, Pd-PdS₂-Co_{4.0} demonstrates the largest voltage decrease. Specifically, the GOR||CO₂RR pair on Pd-PdS₂-Co_{4.0} only necessitates 1.26 V (0.92 and 1.12 V) to attain a current density of 5 mA cm⁻² (1 and 3 mA cm⁻²), which is 1.09 V lower than the voltage required for OER||CO₂RR. Moreover, RuO₂ has been employed as the highly active OER catalyst to further contrast with Pd-PdS₂-Co_{4.0} for GOR coupling with CO₂RR. As shown in Figure S31, the potential at a current density of 5 mA cm⁻² between GOR on Pd-PdS₂-Co_{4.0} and OER on RuO₂ also displays a significant reduction of approximately 0.97 V. Additionally, the voltage drop value of the GOR||CO₂RR pair on Pd-PdS₂-Co_{4.0} also stands out among those state-of-the-art systems coupling CO₂RR with other anodic reactions on various catalysts (Figure S32),^[35–48] suggesting a substantial decrease in electricity consumption.

To further investigate the electricity consumption, we calculated the power densities at the current density of 5 mA cm⁻² in GOR||CO₂RR and OER||CO₂RR, respectively. A comparison between OER||CO₂RR and GOR||CO₂RR on Pd-PdS₂-Co_x reveals a notable decrease in the power density. Specifically, the power density of Pd-PdS₂-Co_{4.0} during GOR||CO₂RR shows the largest reduction at 46.4%, indicating a significant decrease in electrical energy consumption (Figure 5f). This decline in power density highlights the

potential for improved energy efficiency in GOR||CO₂RR compared to OER||CO₂RR. In addition, Pd–PdS₂–Co_{4.0} was found to have the lowest power density for GOR||CO₂RR at various current densities among the catalysts examined, indicating minimal electrical energy consumption (Figure S33). Furthermore, the power density for GOR||CO₂RR on Pd–PdS₂–Co_{4.0} shows slow growth with increasing current density compared to traditional OER||CO₂RR (Figure S34). This suggests that substituting OER with GOR on Pd–PdS₂–Co_{4.0} can significantly decrease the electrical energy consumption for the electrochemical CO₂RR process.

Considering that HCOOH is the primary target product in both the anode and cathode of GOR||CO₂RR, we utilized the potentiostatic method to determine the FE for HCOOH through nuclear magnetic resonance (NMR) spectroscopy (Figures S35–S37). As illustrated in Figures 5g and S38, the anodic FE of HCOOH on Pd–PdS₂–Co_x is significantly higher than that of Pd/C and Pd–PdS₂. Notably, among these catalysts, Pd–PdS₂–Co_{4.0} demonstrates the highest FE toward HCOOH, with the value remaining approximately 90% from 1.5 to 2.4 V on Pd–PdS₂–Co_{4.0}. This suggests superior activity for the conversion of glycerol to formic acid. Moreover, the electrochemical CO₂RR process has been significantly enhanced when coupled with anodic GOR. The cathodic Faradaic efficiency of HCOOH in GOR||CO₂RR process is increased compared to OER||CO₂RR (Figures 5h, S39, and S40). Specifically, the production of HCOOH can be obtained in the low potential region from 1.2 to 1.8 V benefiting from the reduction of cell voltage, which is essential for converting CO₂ into value-added products requiring less electrical energy. Figures 5i, S41, and S42 display the total FE of HCOOH in GOR||CO₂RR and OER||CO₂RR pairs on various catalysts, respectively. Note that the GOR||CO₂RR process employing the Pd–PdS₂–Co_{4.0} catalyst demonstrates a significant advantage in the production of HCOOH. Especially at low voltage levels (1.2–1.8 V), the FE of HCOOH over Pd–PdS₂–Co_{4.0} is more than three times higher than that of Pd/C. Overall, the Pd–PdS₂–Co_{4.0} catalyst exhibits the highest FE and formation rate of HCOOH, as well as current density, while consuming the least amount of electricity compared to other catalysts (Figure 5j). These results confirm the practicality and efficiency of utilizing GOR||CO₂RR for HCOOH production. The durability test for Pd–PdS₂–Co_{4.0} at the cell voltage of 2.1 V was also conducted (Figure S43). The FE of HCOOH in the anode and cathode can maintain ~85% and 70% after running 10 h, respectively. Additionally, the Pd–PdS₂–Co_{4.0} also exhibited excellent long-term stability under harsh conditions (3.0 V, 333 K), retaining ~67% of its initial current density over 24 h (Figure S44), demonstrating its robustness at high voltage and temperature. Besides, the samples collected after the stability test were subjected to TEM analysis. As shown in Figure S45, the morphology of the nanosheet was largely preserved, but several Pd–PdS₂–Co_{4.0} were aggregated. Moreover, the spin state of Co in the Pd–PdS₂–Co_{4.0} catalyst was also analyzed after the GOR process. As shown in Figure S46, there is a slight change in the spin state of Co following the GOR process. Specifically, the percentage of LS state decreases from 68.4% to 60.2%. It is likely due to electron transfer and slight structural changes of

the Pd–PdS₂–Co_{4.0} during the electrochemical GOR process. Nevertheless, Co–LS remains the dominant in Pd–PdS₂–Co_{4.0} after the GOR process, suggesting that the spin state of Co is well preserved.

Conclusion

In summary, we have demonstrated a general method for the synthesis of a series of Pd–PdS₂–Co_x HNSs with tunable Co content. Magnetic characterization confirms the regulated spin state of Co^{III}, i.e., Pd–PdS₂–Co_{4.0} < Pd–PdS₂–Co_{2.8} < Pd–PdS₂–Co_{5.2}, forming ideal models to study how the spin states of Co affect neighboring Pd sites. Based on DFT calculations and Dewar–Chatt–Duncanson model theory, we propose the mechanism of “spin-selective electron donation” for modulating the *d* orbital states of Pd. Co–LS can specifically modify the *d*_{z²} state of Pd through σ -donation via Co–S–Pd bridges, while Co–HS plays a crucial role in regulating the *d*_{xy} state of Pd by π -donation. Profiting by the optimized *d*_{z²} state of Pd, Pd–PdS₂–Co_{4.0} exhibits the excellent performance of bio-alcohols (ethanol, ethylene glycol, and glycerol) electrooxidation with strong ability of C–C bond cleavage. Furthermore, in the GOR||CO₂RR H-type cell, Pd–PdS₂–Co_{4.0} delivers the lowest cell voltage and highest FE of HCOOH. The electrical energy consumption was observed to drop by approximately 46% compared to a traditional OER||CO₂RR system, with the FE of HCOOH reaching ~90% at the anode. Our findings propose the innovative “spin-selective electron donation” strategy, providing a flexible and effective approach to modulate the electron orbital states of active sites.

Acknowledgements

This work was financially supported by National Natural Science Foundation of China (NSFC, 22209039, 22071172, 22375142, 52373233). 2022 Subsidized Project of Tianjin University Graduate Arts and Science Excellence Innovation Award Program (B2-2022-002), Innovation Funding Project of Science and Technology, China National Petroleum Corporation (2022DQ02-0408), the SIAT International Joint Lab Project (No. E3G113), and Shenzhen Science and Technology Program (KQTD20221101093647058). Top-notch Personnel Fund of Henan Agricultural University (30500682). China Postdoctoral Science Foundation under Grant Number 2023M743670 and the Postdoctoral Fellowship Program of CPSF under Grant Number GZC20232867.

Conflict of Interests

The authors declare no conflict of interest.

Data Availability Statement

The data that support the findings of this study are available from the corresponding author upon reasonable request.

Keywords: C—C bond cleavage • Glycerol oxidation reaction • Pd—PdS₂—Co heterostructural nanosheets • Spin state regulation • Spin-selective electron donation

- [1] S. Jin, J. M. Kevin, A. G. Hubert, B. G. John, S.-H. Yang, *Science* **2011**, 334, 1383–1385.
- [2] D. Eum, B. Kim, J.-H. Song, H. Park, H.-Y. Jang, S. J. Kim, S.-P. Cho, M. H. Lee, J. H. Heo, J. Park, Y. Ko, S. K. Park, J. Kim, K. Oh, D. Kim, S. J. Kang, K. Kang, *Nat. Mater.* **2022**, 21, 664–672.
- [3] S. Yao, S. Wang, Y. Liu, Z. Hou, J. Wang, X. Gao, Y. Sun, W. Fu, K. Nie, J. Xie, Z. Yang, Y.-M. Yan, *J. Am. Chem. Soc.* **2023**, 145, 26699–26710.
- [4] Y. Zhou, Q. Gu, K. Yin, L. Tao, Y. Li, H. Tan, Y. Yang, S. Guo, *Proc. Natl. Acad. Sci. USA* **2023**, 120, e2301439120.
- [5] H. Jonathan, R. R. Reshma, G. Livia, K. Yu, Y. Yang, S.-H. Yang, *Science* **2017**, 358, 751–756.
- [6] K. Zhang, A. Cao, L. H. Wandall, J. Vernieres, J. Kibsgaard, J. K. Nørskov, I. Chorkendorff, *Science* **2024**, 383, 1357–1363.
- [7] A. Cao, J. K. Nørskov, *ACS Catal.* **2023**, 13, 3456–3462.
- [8] K. Sun, Y. Huang, Q. Wang, W. Zhao, X. Zheng, J. Jiang, H.-L. Jiang, *J. Am. Chem. Soc.* **2024**, 146, 3241–3249.
- [9] Z. Sun, L. Lin, J. He, D. Ding, T. Wang, J. Li, M. Li, Y. Liu, Y. Li, M. Yuan, B. Huang, H. Li, G. Sun, *J. Am. Chem. Soc.* **2022**, 144, 8204–8213.
- [10] T. Sun, Z. Tang, W. Zang, Z. Li, J. Li, Z. Li, L. Cao, J. S. D. Rodriguez, C. O. M. Mariano, H. Xu, P. Lyu, X. Hai, H. Lin, X. Sheng, J. Shi, Y. Zheng, Y.-R. Lu, Q. He, J. Chen, K. S. Novoselov, C.-H. Chuang, S. Xi, X. Luo, J. Lu, *Nat. Nanotechnol.* **2023**, 18, 763–771.
- [11] T. Li, Y. Deng, X. Rong, C. He, M. Zhou, Y. Tang, H. Zhou, C. Cheng, C. Zhao, *SmartMat.* **2023**, 4, e1142.
- [12] A. Cao, V. J. Bukas, V. Shadravan, Z. Wang, H. Li, J. Kibsgaard, I. Chorkendorff, J. K. Nørskov, *Nat. Commun.* **2022**, 13, 2382.
- [13] S. Verma, S. Lu, P. J. A. Kenis, *Nat. Energy* **2019**, 4, 466–474.
- [14] W. Chen, L. Zhang, L. Xu, Y. He, H. Pang, S. Y. Wang, Y. Zou, *Nat. Commun.* **2024**, 15, 2420.
- [15] R.-Y. Fan, X.-J. Zhai, W.-Z. Qiao, Y.-S. Zhang, N. Yu, N. Xu, Q.-X. Lv, Y.-M. Chai, B. Dong, *Nano-Micro Lett.* **2023**, 15, 190.
- [16] A. Zalineeva, A. Serov, M. Padilla, U. Martinez, K. Artyushkova, S. Baranton, C. Coutanceau, P. B. Atanassov, *J. Am. Chem. Soc.* **2014**, 136, 3937–3945.
- [17] M. Simões, S. Baranton, C. Coutanceau, *Appl. Catal. B-environ* **2010**, 93, 354–362.
- [18] E. A. Monyoncho, S. N. Steinmann, C. Michel, E. A. Baranova, T. K. Woo, P. Sautet, *ACS Catal.* **2016**, 6, 4894–4906.
- [19] Y. Qin, W. Zhang, F. Wang, J. Li, J. Ye, X. Sheng, C. Li, X. Liang, P. Liu, X. Wang, X. Zheng, Y. Ren, C. Xu, Z. Zhang, *Angew. Chem., Int. Ed.* **2022**, 61, e202200899.
- [20] Y. Qin, F. Wang, P. Liu, J. Ye, Q. Wang, Y. Wang, G. Jiang, L. Liu, P. Zhang, X. Liu, X. Zheng, Y. Ren, J. Li, Z. Zhang, *Sci. China Chem.* **2024**, 67, 696–704.
- [21] Y. K. Kim, N. H. Sung, J. D. Denlinger, B. J. Kim, *Nat. Physics* **2016**, 12, 37–41.
- [22] Y. Shi, Y. Guo, Y. Shirako, W. Yi, X. Wang, A. A. Belik, Y. Matsushita, H. L. Feng, Y. Tsujimoto, M. Arai, N. Wang, M. Akaogi, K. Yamaura, *J. Am. Chem. Soc.* **2013**, 135, 16507–16516.
- [23] M. Li, C. Wang, K. Davey, J. Li, G. Li, S. Zhang, J. Mao, Z. Guo, *SmartMat.* **2023**, 4, e1185.
- [24] Y. Chen, Y. M. Lu, H. Y. Kee, *Nat. Commun.* **2015**, 6, 6593.
- [25] Z. C. Chen, Q. Ouyang, W. Du, Y. C. Chen, *J. Am. Chem. Soc.* **2024**, 146, 6422–6437.
- [26] B. A. Smith, K. D. Vogiatzis, *J. Phys. Chem. A* **2021**, 125, 7956–7966.
- [27] S. Guo, S. Dong, E. Wang, *ACS Nano* **2010**, 4, 547–555.
- [28] Z. Liang, L. Song, S. Deng, Y. Zhu, E. Stavitski, R. R. Adzic, J. Chen, J.X. Wang, *J. Am. Chem. Soc.* **2019**, 141, 9629–9636.
- [29] L. Huang, J.-Y. Sun, S.-H. Cao, M. Zhan, Z.-R. Ni, H.-J. Sun, Z. Chen, Z.-Y. Zhou, E. G. Sorte, Y. J. Tong, S.-G. Sun, *ACS Catal.* **2016**, 6, 7686–7695.
- [30] L. Fan, Y. Ji, G. Wang, J. Chen, K. Chen, X. Liu, Z. Wen, *J. Am. Chem. Soc.* **2022**, 144, 7224–7235.
- [31] C. Y. Zhang, C. Zhang, G. W. Sun, J. L. Pan, L. Gong, G. Z. Sun, J. J. Biendicho, L. Balcells, X. L. Fan, J. R. Morante, J. Y. Zhou, A. Cabot, *Angew. Chem., Int. Ed.* **2022**, 61, e202211570.
- [32] S. Mugiraneza, A. M. Hallas, *Commun. Phys.* **2022**, 5, 95.
- [33] J. Chen, *Surf. Sci. Rep.* **1997**, 30, 1–152.
- [34] S. Chen, Z. Kang, X. Hu, X. Zhang, H. Wang, J. Xie, X. Zheng, W. Yan, B. Pan, Y. Xie, *Adv. Mater.* **2017**, 29, 1701687.
- [35] D. D. Ma, S. G. Han, S. H. Zhou, W. B. Wei, X. Li, B. Chen, X. T. Wu, Q. L. Zhu, *CCS Chem.* **2023**, 5, 1827–1840.
- [36] X. Teng, K. Shi, L. Chen, J. Shi, *Angew. Chem., Int. Ed.* **2024**, 63, e202318585.
- [37] D. Wu, J. Hao, Z. Song, X. Z. Fu, J. L. Luo, *Chem. Eng. J.* **2021**, 412, 127893.
- [38] X. Wei, Y. Li, L. Chen, J. Shi, *Angew. Chem., Int. Ed.* **2021**, 60, 3148–3155.
- [39] A. Saxena, S. Kapila, J. E. Medvedeva, M. Nath, *ACS Appl. Mater. Interfaces* **2023**, 15, 14433–14446.
- [40] Y. Pei, Z. Pi, H. Zhong, J. Cheng, F. Jin, *J. Mater. Chem. A* **2022**, 10, 1309–1319.
- [41] C. Cao, D. D. Ma, J. Jia, Q. Xu, X. T. Wu, Q. L. Zhu, *Adv. Mater.* **2021**, 33, e2008631.
- [42] J. Wang, X. Li, M. Wang, T. Zhang, X. Chai, J. Lu, T. Wang, Y. Zhao, D. Ma, *ACS Catal.* **2022**, 12, 6722–6728.
- [43] F. Ye, S. Zhang, Q. Cheng, Y. Long, D. Liu, R. Paul, Y. Fang, Y. Su, L. Qu, L. Dai, C. Hu, *Nat. Commun.* **2023**, 14, 2040.
- [44] J. Li, Y. Zhang, L. Zhang, Q. Zhou, J. Yang, Y. Fu, L. Yu, Y. Sun, Z. Li, Y. Qin, D. Yi, H. Zhang, D. Wang, Z. Zhang, *Angew. Chem., Int. Ed.* **2025**, 64, e202425006.
- [45] Z. Jiang, S. Ren, X. Cao, Q. Fan, R. Yu, J. Yang, J. Mao, *Angew. Chem., Int. Ed.* **2024**, 63, e202408412.
- [46] Y. He, Z. Ma, F. Yan, C. Zhu, T. Shen, S. Chou, X. Zhang, Y. Chen, *Proc. Natl. Acad. Sci. U.S.A.* **2024**, 121, e2320777121.
- [47] H. Chen, R.-T. Gao, K. Su, Z. Li, L. Wu, L. Wang, *Angew. Chem., Int. Ed.* **2025**, 64, e202501766.
- [48] C. Li, H. Li, B. Zhang, H. Li, Y. Wang, X. Wang, P. Das, Y. Li, X. Wu, Y. Li, Y. Cui, J. Xiao, Z.-S. Wu, *Angew. Chem., Int. Ed.* **2024**, 63, e202411542.

Manuscript received: March 15, 2025

Revised manuscript received: April 18, 2025

Accepted manuscript online: April 24, 2025

Version of record online: ■■■■■

Research Article

Glycerol Electrooxidation

P. Liu, H. Ma, Y. Qin*, J. Li, F. Li, J. Ye,
Q. Guo, N. Su, C. Gao, L. Xie, X. Sheng,
S. Zhao, G. Jiang, Y. Ren, Y. Sun*,
Z. Zhang* ————— e202506032

Enhancing C—C Bond Cleavage of Glycerol
Electrooxidation Through Spin-Selective
Electron Donation in Pd–PdS₂–Co_x
Heterostructural Nanosheets

The “spin-selective electron donation” strategy effectively modulates the electronic states of Pd's *d* orbitals (*d*_{z²} and *d*_{xy}) through distinct pathway: σ -donation from low-spin Co^{III} (*t*_{2g}⁶*e*_g⁰) and π -donation from high-spin Co^{III} (*t*_{2g}⁵*e*_g¹).

